

SIMULATIONS OF BINARY NEUTRON STARS AND BLACK HOLE–TORUS SYSTEMS IN GENERAL RELATIVITY*

JOSÉ A. FONT

Departamento de Astronomía y Astrofísica, Universitat de València
Dr. Moliner 50, 46100 Burjassot, Spain

(Received November 6, 2012)

Merging binary neutron stars are among the strongest known sources of gravitational waves, have features compatible with the events producing short-hard gamma-ray bursts, and might be the long-sought formation sites of high-mass number r-process elements. Numerical relativity has reached a stage where a complete description of the inspiral, merger and post-merger phases of the late evolution of close binary neutron-star systems is possible. This is allowing the systematic investigation of such a many-sided subject. This paper presents an overview of numerical relativity simulations of binary neutron star mergers and the evolution of the resulting black hole–torus systems. Such numerical work is based upon a basic theoretical framework which comprises the Einstein’s equations for the gravitational field and the hydrodynamics equations for the evolution of the matter fields. The most well-established formulations for both systems of equations are briefly discussed, along with the numerical methods best suited for their numerical solution, specifically high-order finite-differencing for the case of the gravitational field equations and high-resolution shock-capturing schemes for the case of the relativistic Euler equations. A number of recent results are reviewed, namely the outcome of the merger depending on the initial total mass and equation of state of the binary, as well as the post-merger evolution phase once a black hole–torus system is produced. Such system has been shown to be subject to non-axisymmetric instabilities leading to the emission of large amplitude gravitational waves.

DOI:10.5506/APhysPolB.43.2285

PACS numbers: 04.25.D-, 04.30.-w, 04.40.Dg, 95.30.Lz

* Presented at the LII Cracow School of Theoretical Physics “Astroparticle Physics in the LHC Era”, Zakopane, Poland, May 19–27, 2012.

1. Introduction

For over a decade, there have been many efforts in numerical relativistic astrophysics to simulate the coalescence and merging of binary neutron stars (BNS hereafter). Progress has been steady but somewhat understandably slow, the reason being that the accurate simulation of BNS mergers is one of the most challenging ventures in numerical relativity. This scenario involves strong gravitational fields, matter motion with relativistic speeds, strong relativistic shock waves, and extreme magnetic fields. The numerical difficulties are aggravated by the intrinsic multidimensional character of the problem and by the inherent complexities in Einstein's theory of gravity, such as coordinate degrees of freedom and the possible formation of curvature singularities (*e.g.* collapse of matter configurations to black holes). In spite of these obstacles, current simulations have largely extended the scope of the early works. A number of factors have made this possible: improvements on the mathematical aspects (formulation of the equations), on the physical aspects (incorporation of equations of state (EOS) from nuclear physics), on the numerical aspects (use of high-resolution methods and adaptive mesh refinement) and on the computational aspects (increased computational resources). Large initial separations can now be considered and some of the existing simulations have expanded the dynamical range spanned by the models well beyond black hole formation (see *e.g.* [1–10] and references therein).

These efforts are allowing the computation of the entire gravitational waveform for the first time, from the early inspiral to the decaying tail of the late ringing of the formed black hole. The generation of reliable gravitational wave templates from BNS mergers has become one of the most urgent needs for data analysis groups eager to anticipate the expected signals through computations which strongly rely on matched filtering techniques. The sense of urgency is revealed by the major advances accomplished on the experimental front — the two major interferometer detectors (LIGO and Virgo) have already taken data at the original design sensitivity and are presently undergoing significant upgrades. In addition, the path for research in gravitational wave physics beyond the advanced detectors foresees the Earth-bound Einstein Telescope (ET) as a major large-scale project (costs on the billion Euro scale), whose construction would start at the end of the decade and after the first detection with the advanced detectors. The ASPERA organization¹, a European network of national agencies responsible for coordinating and funding national research efforts in Astroparticle Physics, includes ET in the Magnificent Seven list in its roadmap. ASPERA considers ET one of the “*few projects whose funding has to be kept at sub-*

¹ www.aspera-eu.org

stantial levels, be it because they have an impressive momentum that needs to be maintained, because they enter a phase with high discovery potential, because they go hand in hand with LHC physics, because they are technologically ready and have a worldwide community behind them, or finally, because a delay of crucial decisions and funding could even jeopardize the project.”

In addition to being regarded as the only option to build templates of gravitational waves for the most dynamical phase of the merger itself, the second major incentive to perform BNS simulations is to establish whether the end-product of the merger can be regarded as the underlying mechanism operating at the central engine of short-hard gamma-ray bursts (GRBs) [11, 12]. The consensus emerging from the existing simulations indicates the formation, depending on the suitability of the initial parameters of the simulated model, of a black hole of stellar mass surrounded by a dense hot disk. Driven by neutrino processes and magnetic fields such a compact system may be capable of launching a relativistic fireball with an energy of $\sim 10^{48}$ erg on a timescale of 0.1–1 s [13].

This article presents an overview of the theoretical physical framework upon which most of today’s BNS simulations are based, along with a brief description of the numerical tools employed. A glimpse of the basic facts occurring during a BNS event and during its final outcome, once a black hole surrounded by a dense, thick torus has been produced, will be given to close the article. There exists recent literature, where the topic of this paper is discussed at greater length, *e.g.* references [14–16], and which the interested reader may want to look at.

2. Theoretical model

Compressible fluid dynamics plays a central role in many numerical applications of Computational Astrophysics, as most astrophysical objects (planets, stars, jets, galaxies, *etc.*), as well as the ISM and the IGM can be modelled at a theoretical level as fluids or plasmas. In the context of relativistic astrophysics, general relativity is a key player to describe the physics and dynamics of compact objects (*i.e.* white dwarfs, neutron stars, and black holes). Some of the distinctive scenarios of relativistic astrophysics being explored by numerical relativity are core collapse supernovae leading to neutron stars or black holes, GRBs, accretion on to compact objects, the launching of relativistic jets in AGNs, and the coalescence of compact neutron star (and black hole) binaries.

A powerful way to improve our understanding of these scenarios is through *numerical simulations*. The equations governing the dynamics of relativistic astrophysical systems are an intricate, coupled system of time-dependent partial differential equations, comprising the general relativis-

tic hydrodynamics equations and the Einstein gravitational field equations. In some situations the “test-fluid” approximation, in which the fluid’s self-gravity is neglected against the background gravitational field, may provide an accurate description of the dynamics. Additionally, a description employing ideal hydrodynamics (inviscid fluids) is also commonly used in numerical astrophysics. On the other hand, there are situations, where the number of equations must however be augmented to account for *e.g.* magnetic field effects, radiative processes or improved microphysics (realistic EOS for nuclear matter and nuclear physics). We limit the following discussion to the basic set of theoretical tools necessary to perform numerical simulations in relativistic astrophysics — the hydrodynamics equations and the gravitational field equations. The interested reader is addressed to [14, 16–19] and references therein for details additional to the ones covered here.

2.1. General relativistic hydrodynamics equations

In general relativity, the hydrodynamics equations are obtained from the local conservation laws of the stress-energy tensor and of the matter current density (continuity equation)

$$\nabla_{\mu}(\rho u^{\mu}) = 0, \quad \nabla_{\mu}T^{\mu\nu} = 0. \quad (1)$$

As usual, the Greek indices appearing in the previous equations run from 0 to 3. Moreover, ∇_{μ} is the covariant derivative associated with the spacetime 4-metric $g_{\mu\nu}$. The density current is given by $J^{\mu} = \rho u^{\mu}$, with u^{μ} representing the fluid 4-velocity and ρ the rest-mass density in a locally inertial reference frame.

The stress-energy tensor for a non-perfect fluid is defined as

$$T^{\mu\nu} = \rho(1 + \varepsilon)u^{\mu}u^{\nu} + (p - \mu\Theta)h^{\mu\nu} - 2\xi\sigma^{\mu\nu} + q^{\mu}u^{\nu} + q^{\nu}u^{\mu}, \quad (2)$$

where ε is the specific internal energy density, p is the pressure, $h^{\mu\nu}$ is the spatial projection tensor, $h^{\mu\nu} = u^{\mu}u^{\nu} + g^{\mu\nu}$, and q^{μ} is the energy flux. In addition, μ and ξ are the shear and bulk viscosity coefficients. The expansion, Θ , describing the divergence or convergence of the fluid world lines is defined as $\Theta = \nabla_{\mu}u^{\mu}$. The symmetric, trace-free, and spatial shear tensor $\sigma^{\mu\nu}$ is defined by

$$\sigma^{\mu\nu} = \frac{1}{2}(\nabla_{\alpha}u^{\mu}h^{\alpha\nu} + \nabla_{\alpha}u^{\nu}h^{\alpha\mu}) - \frac{1}{3}\Theta h^{\mu\nu}. \quad (3)$$

In what follows, we neglect non-adiabatic effects, such as viscosity or heat transfer, assuming the stress-energy tensor to be that of a perfect fluid

$$T^{\mu\nu} = \rho h u^{\mu} u^{\nu} + p g^{\mu\nu}, \quad (4)$$

where we have introduced the relativistic specific enthalpy, defined as $h = 1 + \varepsilon + p/\rho$. Introducing an explicit coordinate chart, the previous conservation equations read

$$\frac{\partial}{\partial x^\mu} (\sqrt{-g} \rho u^\mu) = 0, \quad (5)$$

$$\frac{\partial}{\partial x^\mu} (\sqrt{-g} T^{\mu\nu}) = \sqrt{-g} \Gamma_{\mu\lambda}^\nu T^{\mu\lambda}, \quad (6)$$

where the scalar x^0 is used to define the foliation of the spacetime with hypersurfaces (with coordinates x^i ; Latin indices run from 1 to 3). In the previous equations, $g = \det(g_{\mu\nu})$ and $\Gamma_{\mu\lambda}^\nu$ are the so-called Christoffel symbols.

The system formed by the equations of motion and the continuity equation must be supplemented with an EOS relating the pressure to some fundamental thermodynamical quantities, *e.g.* $p = p(\rho, \varepsilon)$. In the test-fluid approximation the dynamics of the matter fields is fully described by the previous conservation laws and the EOS. When such approximation does not hold, the previous equations must be solved in conjunction with Einstein's equations for the gravitational field which describe the evolution of a dynamical spacetime. Those will be discussed in the next section.

There exist different formulations to cast the conservation equations into forms suitable for numerical work. Those depend on

- The choice of slicing of the spacetime, namely the level surfaces of x^0 can be spatial (as in the 3+1 approach of general relativity) or null (as in the characteristic initial value problem of general relativity).
- The choice of physical (primitive) variables $(\rho, \varepsilon, u^i, \dots)$ to carry out the mathematical analysis of the system of equations.

The hydrodynamics equations were written as a set of advection equation within the 3+1 formalism by Wilson in 1972 [20]. This approach sidesteps an important guideline for the formulation of nonlinear hyperbolic systems of equations, the preservation of their conservation form. This is a necessary feature to guarantee a correct evolution in regions of entropy generation (*i.e.* shocks). As a result, some amount of numerical dissipation (artificial viscosity) must be used to stabilize the numerical solution across discontinuities. Conservative formulations well-adapted to numerical methodology were developed in the 1990s, see [18, 21–23].

Numerically, the hyperbolic and conservative nature of the general relativistic hydrodynamics equations allows to design a solution procedure based on the characteristic speeds and fields of the system, translating to relativistic hydrodynamics existing tools of Computational Fluid Dynamics.

The extension of modern high-resolution shock-capturing (HRSC) schemes from classical fluid dynamics to relativistic hydrodynamics was accomplished in three steps:

- Casting the equations as a system of conservation laws.
- Identifying the suitable vector of unknowns.
- Building up an approximate Riemann solver.

The associated numerical scheme has to meet a key prerequisite — being written in conservation form, as this automatically guarantees the correct propagation of discontinuities as well as the correct Rankine–Hugoniot (jump) conditions across discontinuities (the shock-capturing property). In 1991, Martí, Ibáñez, and Miralles presented a new formulation of the general relativistic hydrodynamics equations, in 1+1, aimed at taking advantage of their hyperbolic character [21]. The corresponding 3+1 extension was presented in [24] in special relativity and in [18] in general relativity. Details on the derivation of the equations can be found in the previous references. Here, we simply summarise the resulting first-order, flux-conservative hyperbolic system of equations well-adapted to numerical methodology

$$\frac{1}{\sqrt{-g}} \left(\frac{\partial \sqrt{\gamma} \mathbf{U}}{\partial x^0} + \frac{\partial \sqrt{-g} \mathbf{F}^i}{\partial x^i} \right) = \mathbf{S}, \quad (7)$$

where the state vector \mathbf{U} and the vectors of fluxes \mathbf{F}^i and sources \mathbf{S} are respectively given by

$$\mathbf{U} = (D, S_j, \tau), \quad (8)$$

$$\mathbf{F}^i = \left(D \left(v^i - \frac{\beta^i}{\alpha} \right), S_j \left(v^i - \frac{\beta^i}{\alpha} \right) + p \delta_j^i, \tau \left(v^i - \frac{\beta^i}{\alpha} \right) + p v^i \right), \quad (9)$$

$$\mathbf{S} = \left(0, T^{\mu\nu} \left(\frac{\partial g_{\nu j}}{\partial x^\mu} - \Gamma_{\nu\mu}^\delta g_{\delta j} \right), \alpha \left(T^{\mu 0} \frac{\partial \ln \alpha}{\partial x^\mu} - T^{\mu\nu} \Gamma_{\nu\mu}^0 \right) \right). \quad (10)$$

The state vector comprises the relativistic densities of mass, momentum, and energy, and are defined as $D = \rho W$, $S_j = \rho h W^2 v_j$ and $\tau = \rho h W^2 - p - D$. In these expressions W is the Lorentz factor of the flow, $W^2 = 1/(1 - v_j v^j)$, with v^j being the 3-velocity of the Eulerian observer, defined as

$$v^i = \frac{1}{\alpha} \left(\frac{u^i}{u^t} + \beta^i \right). \quad (11)$$

In many of the above equations appear the quantities α and β^i . This is a consequence of the fact that we are implicitly using the so-called 3+1 formulation of general relativity in the derivation of the hydrodynamics

equations (see *e.g.* [16] and references therein for details). In this formulation, spacetime is foliated with a set of non-intersecting spacelike hypersurfaces Σ . Within a given hypersurface, distances are measured with the spatial 3-metric γ_{ij} . There are two kinematical variables that describe the evolution from one hypersurface to the next: the lapse function α which describes the rate of proper time along a timelike unit vector n^μ normal to the hypersurface, and the shift vector β^i , spatial vector which describes the movement of coordinates in the hypersurface. The line element of the spacetime is then given by the following expression

$$ds^2 = -(\alpha^2 - \beta_i \beta^i) dt^2 + 2\beta_i dx^i dt + \gamma_{ij} dx^i dx^j. \quad (12)$$

Hyperbolic conservation laws such as Eq. (7) are accurately solved by employing HRSC numerical schemes. These schemes are based on approximate Riemann solvers that make explicit use of the local characteristic structure of the hyperbolic system of equations. For the relativistic hydrodynamics equations this information was reported in [18]. The eigenvalues (characteristic speeds) are all real (but not distinct, one showing a threefold degeneracy), and there exists a complete set of right-eigenvectors. The above system satisfies, hence, the mathematical definition of hyperbolicity. The interested reader is addressed to [14] for further details.

2.2. Einstein's equations and Numerical Relativity

The dynamics of the gravitational field is described by Einstein's field equations

$$G_{\mu\nu} \equiv R_{\mu\nu} - \frac{1}{2}g_{\mu\nu}R = 8\pi T_{\mu\nu}. \quad (13)$$

These equations relate the spacetime geometry (left-hand side) with the distribution of matter and energy (right-hand side). Paraphrasing the relativist John Archibald Wheeler: *Matter tells spacetime how to curve, and spacetime tells matter how to move.* Einstein's equations are a system of 10 nonlinear, coupled, partial differential equations in 4 dimensions. Behind their seemingly inoffensive look when written in covariant form, when they are written with respect to a general coordinate system they may contain hundreds of terms.

There are plenty of exact solutions of Einstein's field equations, but very few of such solutions have astrophysical significance. Due to their complexity exact solutions of such equations have only been found when adopting simplifying symmetries:

- Schwarzschild solution (static and spherically symmetric).
- Kerr solution (stationary and axisymmetric).
- Cosmological solutions (isotropic, homogeneous, or both).

When dealing with more complex systems with astrophysical significance (*e.g.* gravitational collapse or mergers of compact binaries) is not feasible to solve Einstein's equations in an exact way. The field of Numerical Relativity emerged in the mid 1960s from the need to study such kind of astrophysical problems, aiming at trying to solve the field equations with supercomputers using numerical approximations. Nowadays, Numerical Relativity's main goal is to provide templates of the gravitational radiation produced in astrophysical sources to facilitate its detection and the analysis of the available data by the ongoing experiments such as LIGO and Virgo.

To derive a set of equations in a way suitable for 3+1 numerical investigations from the covariant equations given by Eq. (13), we need to start by defining a few geometrical quantities (see *e.g.* [16] for a complete account). First, we need to distinguish between the intrinsic and the extrinsic curvature of the spatial hypersurfaces. While the intrinsic curvature is given by the 3-dimensional Riemann tensor and is defined in terms of the 3-metric γ_{ij} , the extrinsic curvature measures the change of the vector normal to the hypersurface as it is parallel-transported from one point in the hypersurface to another. In order to obtain its mathematical form, we need to define the projection operator

$$P_{\beta}^{\alpha} \equiv \delta_{\beta}^{\alpha} + n^{\alpha}n_{\beta}, \quad (14)$$

where $\delta_{\beta}^{\alpha} = g^{\alpha\mu}g_{\mu\beta}$ and n^{α} is the unit normal vector, which is defined as

$$n^{\mu} = \left(\frac{1}{\alpha}, -\frac{\beta^i}{\alpha} \right), \quad n_{\mu} = (-\alpha, 0), \quad (15)$$

with the normalization condition $n^{\mu}n_{\mu} = -1$. The extrinsic curvature is then defined as

$$K_{\alpha\beta} = -P_{\alpha}^{\mu}P_{\beta}^{\nu}\nabla_{\mu}n_{\nu} = -\nabla_{\alpha}n_{\beta} - n_{\alpha}n^{\mu}\nabla_{\mu}n_{\beta}. \quad (16)$$

Substituting the form of the normal vector in the definition of the extrinsic curvature, we obtain

$$K_{ij} = \frac{1}{2\alpha} (-\partial_t\gamma_{ij} + \nabla_i\beta_j + \nabla_j\beta_i). \quad (17)$$

Using the projection operator and the normal vector, Einstein's equations can be separated in three groups:

- Normal projection (1 equation; energy or Hamiltonian constraint)

$$n^{\alpha}n^{\beta} (G_{\alpha\beta} - 8\pi T_{\alpha\beta}) = 0. \quad (18)$$

- Mixed projections (3 equations; momentum constraints)

$$P^{\mu\alpha} \left[n^\beta (G_{\alpha\beta} - 8\pi T_{\alpha\beta}) \right] = 0. \quad (19)$$

- Projection onto the hypersurface (6 equations; evolution of the extrinsic curvature)

$$P_\alpha^\mu P_\beta^\nu (G_{\mu\nu} - 8\pi T_{\mu\nu}) = 0. \quad (20)$$

After some algebra, it can be shown [16] that the above equations take the following canonical 3+1 form

$$\partial_t \gamma_{ij} = -2\alpha K_{ij} + \nabla_i \beta_j + \nabla_j \beta_i, \quad (21)$$

$$\begin{aligned} \partial_t K_{ij} = & -\nabla_i \nabla_j \alpha + \alpha (R_{ij} + K K_{ij} - 2K_{im} K_j^m) + \beta^m \nabla_m K_{ij} \\ & + K_{im} \nabla_j \beta^m + K_{mj} \nabla_i \beta^m - 8\pi \alpha (T_{ij} - \frac{1}{2} \gamma_{ij} T_m^m + \frac{1}{2} \rho \gamma_{ij}), \end{aligned} \quad (22)$$

and

$$\begin{aligned} R + K^2 - K^{ij} K_{ij} &= 16\pi \rho, \\ \nabla_i (K^{ij} - \gamma^{ij} K) &= 8\pi S^j. \end{aligned} \quad (23)$$

The first group of equations is a set of 12 evolution equations². The first 6 are, in fact, the definition of the extrinsic curvature, Eq. (17), while the remaining 6 describe its time derivative. Correspondingly, the second group of equations is a set of 4 constraint equations. This set of 16 equations constitute what is called the 3+1 formulation of Einstein's equations [25–28]. There are several quantities that need to be defined in the above equations: ∇_i is the covariant derivative with respect to the induced 3-metric, R_{ij} is the Ricci tensor, given by

$$R_{ij} = \partial_n \Gamma_{ij}^n - \partial_j \Gamma_{in}^n + \Gamma_{mn}^n \Gamma_{ij}^m - \Gamma_{jm}^n \Gamma_{in}^m, \quad (24)$$

Γ_{jk}^i are the Christoffel symbols

$$\Gamma_{jk}^i = \frac{1}{2} \gamma^{in} \left(\frac{\partial \gamma_{nj}}{\partial x^k} + \frac{\partial \gamma_{nk}}{\partial x^j} - \frac{\partial \gamma_{jk}}{\partial x^n} \right), \quad (25)$$

$R = R_{ij} \gamma^{ij}$ is the scalar curvature, and $K = K_{ij} \gamma^{ij}$ is the trace of the extrinsic curvature. In addition, some of the terms in the equations contain

² It is also common to encounter these equations written in terms of the so-called Lie derivative, which is a directional derivative that evaluates the change of a given scalar, vector or tensor field along the direction of a vector field (see [16] for details). Using such compact notation Eq. (21) can be written as $(\partial_t - \mathcal{L}_\beta) \gamma_{ij} = -2\alpha K_{ij}$.

the matter fields, which are given by the following definitions:

$$\rho \equiv T^{\mu\nu} n_\mu n_\nu = \rho h W^2 - p, \tag{26}$$

$$S^i \equiv -P_\mu^i T^{\mu\nu} n_\nu = \rho h W^2 v^i, \tag{27}$$

$$S_{ij} \equiv P_i^\mu P_j^\mu T_{\mu\nu} = \rho h W^2 v_i v_j + \gamma_{ij} p, \tag{28}$$

$$S \equiv \rho h W^2 v_i v^i + 3p. \tag{29}$$

The Einstein equations in 3+1 form compose a Cauchy (initial value) problem: first, we need to specify the initial data, γ_{ij} and K_{ij} at the initial slice $t = 0$ subject to the constraint equations. Next, we have to specify the coordinates through the choice of the (freely specifiable) kinematical variables α and β^i . Finally, the initial data are evolved in time using the evolution equations.

In recent years, the 3+1 system has been reformulated into forms better suited for numerical work, aiming at getting rid of unstable evolutions commonly encountered when simulating black hole spacetimes. Among the various choices investigated the so-called BSSN formulation [29–31] has become the preferred choice for most groups. The basic idea to improve the stability of the numerical solutions was to remove the mixed second derivatives in the Ricci tensor by introducing auxiliary variables. By doing this the evolution equations resemble wave equations for the 3-metric and the extrinsic curvature. We start with a conformal decomposition of the 3-metric

$$\tilde{\gamma}_{ij} = \psi^4 \gamma_{ij}, \tag{30}$$

with the condition $\det \tilde{\gamma}_{ij} = 1$. The BSSN evolution variables are then the following ones (notice that the trace of extrinsic curvature is a separate variable)

$$\phi = \frac{1}{4} \log \psi, \quad \tilde{\gamma}_{ij} = e^{-4\phi} \gamma_{ij}, \tag{31}$$

$$K = \gamma^{ij} K_{ij}, \quad \tilde{A}_{ij} = e^{-4\phi} \left(K_{ij} - \frac{1}{3} \gamma_{ij} K \right), \tag{32}$$

together with a new set of evolution variables (gauge source functions)

$$\tilde{\Gamma}^a = \tilde{\gamma}^{ij} \tilde{\Gamma}_{ij}^a = -\partial_i \tilde{\gamma}^{ai}. \tag{33}$$

It can be shown that the final system of evolution equations in the BSSN formulation takes the following form:

$$(\partial_t - \mathcal{L}_\beta) \tilde{\gamma}_{ij} = -2\alpha \tilde{A}_{ij} \tag{34}$$

$$(\partial_t - \mathcal{L}_\beta) \phi = -\frac{1}{6} \alpha K \tag{35}$$

$$(\partial_t - \mathcal{L}_\beta) K = -\gamma^{ij} \nabla_i \nabla_j \alpha + \alpha \left[\tilde{A}_{ij} \tilde{A}^{ij} + \frac{1}{3} K^2 + \frac{1}{2} (\rho + S) \right] \tag{36}$$

$$(\partial_t - \mathcal{L}_\beta)\tilde{A}_{ij} = e^{-4\phi} [-\nabla_i \nabla_j \alpha + \alpha (R_{ij} - S_{ij})]^{\text{TF}} \tag{37}$$

$$+ \alpha \left(K \tilde{A}_{ij} - 2 \tilde{A}_{il} \tilde{A}_j^l \right) \tag{38}$$

$$(\partial_t - \mathcal{L}_\beta)\tilde{\Gamma}^i = -2\tilde{A}^{ij}\partial_j\alpha + 2\alpha \left(\tilde{\Gamma}_{jk}^i \tilde{A}^{kj} - \frac{2}{3}\tilde{\gamma}^{ij}\partial_j K - \tilde{\gamma}^{ij}S_j + 6\tilde{A}^{ij}\partial_j\phi \right) + \partial_j \left(\beta^l \tilde{\partial}_l \gamma^{ij} - 2\tilde{\gamma}^{m(j}\partial_m\beta^{i)} + \frac{2}{3}\tilde{\gamma}^{ij}\partial_l\beta^l \right). \tag{39}$$

Despite the augmented number of evolution equations with respect to the 3+1 system, BSSN is currently the standard 3+1 formulation in Numerical Relativity. Long-term stable applications have been achieved with this system, including strongly gravitating systems such as neutron stars (both isolated and binaries) and, remarkably, single and binary black holes.

2.3. Numerical methods for conservation laws

There are a variety of numerical methods to solve the equations of fluid dynamics, either classical or relativistic. Among the main schemes we can list the following:

- Finite difference methods. Require numerical viscosity to stabilize the solution in regions where discontinuities develop.
- Finite volume methods. Written in conservation form. Use Riemann solvers to solve the equations in the presence of discontinuities and are commonly known as high-resolution shock-capturing schemes.
- Symmetric methods. Written in conservation form. Based on centred finite differences and high spatial order.
- Particle methods. Smoothed Particle Hydrodynamics [32]. Integrate movement of discrete particles to describe the flow.

Just as their Newtonian counterparts, the equations of general relativistic hydrodynamics is nonlinear hyperbolic system of conservation laws. A distinctive feature of such systems is that smooth initial data can develop discontinuities during the time evolution. Finite difference schemes may show important deficiencies when dealing with such systems. Typically, first order accurate schemes are too dissipative across discontinuities while second order (or higher) schemes produce spurious oscillations near discontinuities [33].

Finite difference schemes provide numerical solutions of the discretised version of the partial differential equations (PDEs). Therefore, convergence properties under grid refinement must be enforced on such schemes to guarantee the validity of the numerical result. The Lax–Wendroff theorem states

that for hyperbolic systems of conservation laws, schemes written in *conservation form* converge to one of the so-called *weak solutions* of the PDEs (C^1 solutions in smooth parts of the flow and with a finite number of discontinuities). However, the class of all weak solutions is too wide as there is no uniqueness for the initial value problem. Thus, among all weak solutions, the numerical scheme must guarantee convergence to the *physically admissible solution*, a property whose mathematical characterisation was given by Lax for hyperbolic systems of conservation laws.

A conservative scheme for the hyperbolic system (7) can be straightforwardly devised by using the corresponding integral form

$$\int_{\Omega} \frac{1}{\sqrt{-g}} \frac{\partial \sqrt{\gamma} \mathbf{U}}{\partial x^0} d\Omega + \int_{\Omega} \frac{1}{\sqrt{-g}} \frac{\partial \sqrt{-g} \mathbf{F}^i}{\partial x^i} d\Omega = \int_{\Omega} \mathbf{S} d\Omega, \tag{40}$$

where Ω is a region of the 4-dimensional manifold enclosed within a 3-dimensional surface $\partial\Omega$ which is bounded by two spacelike surfaces $\Sigma_t, \Sigma_{t+\Delta t}$ and two timelike surfaces $\Sigma_{x^i}, \Sigma_{x^i+\Delta x^i}$. For numerical purposes the above relation can be written as

$$\begin{aligned} \bar{U}_{t+\Delta t} - \bar{U}_t = & - \left(\int_{\Sigma_{x^1+\Delta x^1}} \sqrt{-g} \hat{\mathbf{F}}^1 dx^0 dx^2 dx^3 - \int_{\Sigma_{x^1}} \sqrt{-g} \hat{\mathbf{F}}^1 dx^0 dx^2 dx^3 \right) \\ & - \left(\int_{\Sigma_{x^2+\Delta x^2}} \sqrt{-g} \hat{\mathbf{F}}^2 dx^0 dx^1 dx^3 - \int_{\Sigma_{x^2}} \sqrt{-g} \hat{\mathbf{F}}^2 dx^0 dx^1 dx^3 \right) \\ & - \left(\int_{\Sigma_{x^3+\Delta x^3}} \sqrt{-g} \hat{\mathbf{F}}^3 dx^0 dx^1 dx^2 - \int_{\Sigma_{x^3}} \sqrt{-g} \hat{\mathbf{F}}^3 dx^0 dx^1 dx^2 \right) \\ & + \int_{\Omega} \mathbf{S} d\Omega, \end{aligned} \tag{41}$$

where

$$\bar{U} = \frac{1}{\Delta V} \int_{x^1}^{x^1+\Delta x^1} \int_{x^2}^{x^2+\Delta x^2} \int_{x^3}^{x^3+\Delta x^3} \sqrt{\gamma} \mathbf{U} dx^1 dx^2 dx^3 \tag{42}$$

and

$$\Delta V = \int_{x^1}^{x^1+\Delta x^1} \int_{x^2}^{x^2+\Delta x^2} \int_{x^3}^{x^3+\Delta x^3} \sqrt{\gamma} dx^1 dx^2 dx^3. \tag{43}$$

The main advantage of this procedure is that those variables which obey a conservation law are conserved during the evolution, as long as the balance between the fluxes at the boundaries of the computational domain and the source terms are zero. The *numerical fluxes* appearing in Eq. (41) are calculated at cell interfaces where the flow conditions can be discontinuous. Those numerical fluxes are approximations to the time-averaged fluxes across an interface, *i.e.*

$$\hat{\mathbf{F}}_{i+\frac{1}{2}} = \frac{1}{\Delta t} \int_{t^n}^{t^{n+1}} \mathbf{F} \left(\mathbf{U} \left(x_{i+\frac{1}{2}}, t \right) \right) dt, \quad (44)$$

where the flux integral depends on the solution at the numerical interfaces, $\mathbf{U}(x_{i+\frac{1}{2}}, t)$, during the time step. Godunov first proposed to calculate $\mathbf{U}(x_{i+\frac{1}{2}}, t)$ by exactly solving Riemann problems (initial value problems with discontinuous data) at every cell interface to obtain $\mathbf{U}(x_{i+\frac{1}{2}}, t) = \mathbf{U}(0; \mathbf{U}_i^n, \mathbf{U}_{i+1}^n)$, which denotes the Riemann solution for the (left and right) states $\mathbf{U}_i^n, \mathbf{U}_{i+1}^n$ along the ray $x/t = 0$. This procedure had far-reaching consequences as it was incorporated in the design of numerical schemes for solving the Euler equations of classical gas dynamics in the presence of shock waves, which led to major advances in the field. One of the steps in the derivation of the exact Riemann solution involves the computation of the full wave speeds to find where they lie in state space. This is a computationally expensive procedure, which explains the gradual development of *approximate Riemann solvers*, which despite being much cheaper than the exact solver yield equally good results. An excellent introduction to the existing approximate solvers in relativistic hydrodynamics can be found in [34]. We also note that the exact solution of the Riemann problem in *special* relativistic hydrodynamics is reported in [35, 36].

The spatial accuracy of the numerical solution can be increased by reconstructing the primitive variables at the cell interfaces before the actual computation of the numerical fluxes. Diverse cell-reconstruction procedures are available in the literature (see references in [33, 34]). Correspondingly, the temporal accuracy of the scheme is improved by advancing in time the equations in integral form using the method-of-lines in tandem with a high-order, conservative Runge–Kutta method.

For the numerical solution of the subset of evolution equations in Einstein’s field equations the time integration is also performed via a method-of-lines approach. The system of PDEs, which can be cast in hyperbolic form as

$$\partial_t \mathbf{u} + A^i \partial_i \mathbf{u} = \mathbf{s}(\mathbf{u}), \quad (45)$$

can be recast into the form of an ODE in time

$$\partial_t \mathbf{u} = \mathcal{L}(\mathbf{u}), \quad (46)$$

where \mathcal{L} represents a spatial discretization operator. Different numerical methods use different ways to express the spatial derivatives appearing in this operator. The most common choice by far in numerical relativity is to use high-order finite difference approximations for the derivatives, although there are also successful implementations which use spectral expansions and finite elements.

3. Simulations

3.1. Binary neutron star mergers

As mentioned in the introduction, there are quite a few numerical relativity groups worldwide which are nowadays performing increasingly more realistic simulations of BNS (see [15] and references therein for an up-to-date account). Interestingly, the numerical framework upon which most of the simulations are based is becoming standardized. Hence, most of the available codes deal with the gravitational field equations using the BSSN conformal and traceless 3+1 formulation of Einstein's equations as the basic evolution system. As gauge conditions most codes employ 1+log slicing for the lapse function and hyperbolic Gamma-driver for the shift vector evolution. The evolution equations are integrated using high-order schemes, typically 4th to 8th order finite-differencing. As for the initial data, consistent configurations of irrotational BNS in quasi-circular orbit have so far been used. Finally, the gravitational wave-extraction is carried out with two complementary approaches, either using the Newman–Penrose approach which involves the projection of the Weyl tensor onto components of a null tetrad or using gauge-invariant perturbations on a Schwarzschild background expanding the spatial metric into a tensor basis of Regge–Wheeler harmonics (specific details can be found in *e.g.* [37]). Correspondingly, the hydrodynamics equations are solved with the kind of Riemann-solver-based HRSC methods outlined in the preceding section with high order cell reconstruction techniques. The time integration is done with a method-of-lines based on high-order conservative Runge–Kutta algorithms (see [14] for further information).

The seminal studies of BNS mergers in full general relativity carried out by Shibata and co-workers about 10 years ago [38–40] using an ideal fluid EOS, showed that the final outcome of the merger depends in a significant manner on the initial compactness of the neutron stars before plunge. It was found that, depending on the stiffness of the EOS, controlled through the value of the adiabatic index Γ , if the total rest mass of the system is ~ 1.3 – 1.7 times larger than the maximum rest mass of a spherical star in isolation, the end product is a black hole. Otherwise, a marginally-stable massive neutron star forms, supported against self-gravity by rapid differential rotation.

This *hypermassive* neutron star (HMNS) may eventually collapse to a black hole once sufficient angular momentum is dissipated via neutrino emission and/or gravitational radiation. In turn, the different outcome of the merger is imprinted in the gravitational waveforms, as first noted by [40]. Owing to this feature, future detection of high-frequency gravitational waves from a BNS merger event could help constrain the maximum allowed mass of neutron stars along with the composition of neutron star matter. This has been recently scrutinized in simulations performed by the Kyoto group [41, 42] in which a number of new ingredients have been incorporated in the numerical modelling (namely nucleonic and hyperonic finite-temperature EOS and neutrino cooling).

Numerical simulations from the AEI group [2] have also shown that while the qualitative trend taking place during a BNS merger is fairly general (formation of a HMNS followed by the appearance of a black hole–torus system), there are significant quantitative differences in the course of events worth stressing. These differences are produced either by differences in the total mass of the binary for the same EOS or *vice versa*. In the former case a binary with smaller mass (in [2] binaries with total ADM masses of $2.681 M_{\odot}$ and $2.982 M_{\odot}$ were considered) will produce a HMNS which is further away from the stability threshold and will collapse at a later time. In the latter case, a binary with an EOS allowing for a larger thermal internal energy (which will be hotter after merger) will have an increased pressure support and will also collapse at a later time. Moreover, a polytropic EOS leads either to the prompt formation of a rapidly rotating black hole surrounded by a dense torus in the high-mass case, or, in the low-mass case, to a HMNS which develops a bar, emitting large amounts of gravitational radiation until it eventually collapses to a black hole.

Likewise, numerical simulations have also revealed that the key parameter controlling the amount of mass left in the disk for a given initial mass in the system and EOS is the neutron star mass ratio [1, 6, 9, 43]. Namely, the larger the departure from equal-mass ratio, the more important tidal effects become in the less massive star, resulting in its tidal disruption. Since this takes place when the separation is still comparatively large, the angular momentum of the matter is still large and it results in larger-size and more massive disks. Early, low-resolution simulations with an ideal-gas EOS [43] produced a disk mass of several percents of the total mass of the system for a mass ratio of ~ 0.85 . Improved simulations by [1] which adopted a hybrid EOS to mimic realistic, stiff nuclear EOS, indicate that the mass of the disk is $\sim 0.01 M_{\odot}$ or slightly larger in the most favourable case when the merger results in the formation of a marginally-stable HMNS of large ellipticity. Similar disk masses, as large as $\sim 0.02 M_{\odot}$, are also reported in the simulations of [6], in which the initial orbital separation of the two stars is larger

than in previous works. Finally, the most recent investigation of this topic by [9] report that equal-mass binaries do not produce significant tori if they have a total baryonic mass $M_{\text{tot}} \geq 3.7 M_{\odot}$. Those produced have masses $M_{\text{tor}} \sim 10^{-3} M_{\odot}$ and a radial extension of ~ 30 km. Tori with masses as large as $\sim 0.2 M_{\odot}$ have been measured with binaries having $M_{\text{tot}} \sim 3.4 M_{\odot}$ and mass ratios in the range ~ 0.75 – 0.85 . The tori in these cases are much more extended with typical sizes ≥ 120 km. Figure 1, extracted from the work of [9], presents a comparison of the resulting disk morphology following two such illustrative BNS mergers. Both tori differ in size by about a factor 3 and in mass by about a factor 200. However, they have comparable mean rest-mass densities. Overall, the existing literature proves that large-scale tori with large masses and quasi-stationary evolutions can be produced as the result of the inspiral and merger of unequal-mass BNS. Hence, they may indeed provide the energy reservoir needed to power short-hard GRBs.

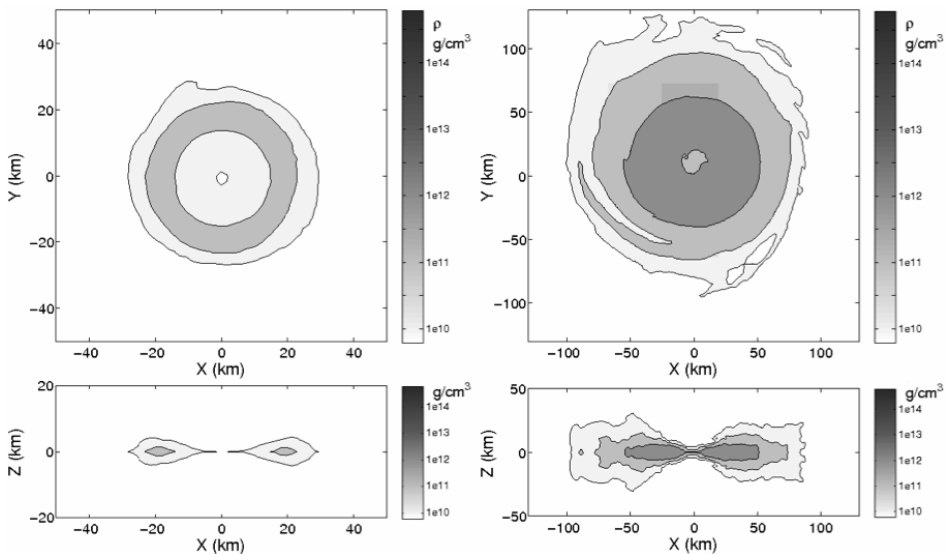


Fig. 1. Isodensity contours for two of the BNS mergers studied in [9]. The left panels show the morphology of the resulting black hole–torus system for a model with equal-mass ratio, while the right panels show the corresponding morphology for a binary with a 0.7 mass ratio between the two stars. The upper rows shows the (x, y) plane and the lower ones show the (x, z) plane. Note that the disks in the two panels have very different lengthscales. The disk resulting from an unequal-mass merger (right panel) is not only ~ 3 larger on the equatorial plane, but it also shows an increased thickness in the vertical direction.

3.2. Black hole–torus systems

Black hole–torus systems are common in the universe. The central region of AGNs is believed to consist of a supermassive black hole of mass $\sim 10^6\text{--}10^{10} M_\odot$ surrounded by a torus. Such systems may form through the collapse of supermassive stars [44, 45]. On the other hand, mergers of neutron star binaries (and black hole–neutron star binaries) often result in a black hole and a torus, as we have just discussed [6, 9]. Moreover, such systems can also be produced at the end of the life of massive stars [46]. The merger and collapsar scenarios are linked to short- and long-duration GRBs, respectively [11, 47].

In a GRB, the energy supply comes from the energy released by the accretion of disk material onto the black hole and from the rotational energy of the black hole itself, which can be extracted, for instance, via the Blandford–Znajek mechanism. This vast amount of energy (of the order of $10^{53}\text{--}10^{54}$ erg, depending on the mass of the disk and on the black hole rotation and mass) is sufficient to power a GRB if the energy released can be converted into gamma-rays with an efficiency of about a few percent. This scenario requires a stable enough system to survive for a few seconds. In particular, the internal-shock model [48] implies that the duration of the energy release by the source has to be comparable with the observed duration of the GRB. Any instability which might disrupt the system on shorter timescales, such as the so-called runaway instability and the Papaloizou–Pringle instability, could pose a severe problem for the accepted GRB models.

In a black hole–torus system the gas flows in an effective (gravitational + centrifugal) potential whose structure is similar to that of a close binary. The Roche torus has a cusp-like inner edge at the Lagrange point L_1 , where mass transfer driven by the radial pressure gradient is possible. These systems may be subject to a runaway instability [49–51]: due to accretion from the disk the black hole mass and spin increase and the gravitational field changes. Two evolutions are feasible to reach a new equilibrium solution: (a) either the cusp moves inwards toward the black hole, slowing down the mass transfer (stable situation), or (b) the cusp moves deeper inside the disk material, speeding up the mass transfer (unstable situation).

Recent axisymmetric numerical relativity simulations by [52] have shown that the runaway instability does not have a significant impact on the dynamics even if the torus self-gravity is taken into account. These simulations use equilibrium configurations of self-gravitating tori around black holes, using the method developed by [53]. The tori built do not overflow their Roche lobes and have both constant and non-constant distributions of the angular momentum. The simulations reveal that such tori are remarkably stable irrespective of the angular momentum distribution.

On the other hand, the fully three-dimensional simulations of [9] show that all black hole–torus systems formed self-consistently as the result of BNS mergers do not manifest signs of any dynamical instability either, at least on the short dynamical timescales investigated by [9]. In particular, it was found that tori formed from equal-mass binaries exhibit a quasi-periodic form of accretion associated with the radial epicyclic oscillations of the tori, while those from unequal-mass binaries exhibit a quasi-steady form of accretion. When analysing the evolution of the angular-momentum distribution in the tori, no evidence for the onset of non-axisymmetric instabilities was found. Moreover, the angular momentum is transported outwards more efficiently for smaller values of the neutron star mass ratio, yielding Keplerian angular-velocity distributions.

However, on longer timescales than those investigated by [9], a non-axisymmetric ($m = 1$) instability may set in. Using perturbation theory, Papaloizou and Pringle [54] first established in 1984 that tori with constant specific angular momentum are unstable to non-axisymmetric global modes. Global unstable modes have a co-rotation radius within the torus, located in a narrow region, where waves cannot propagate. This region separates inner and outer regions, where wave propagation is possible. Waves can tunnel through the co-rotation zone and interact with waves in the other region. Such transmitted modes can be amplified only if there is a feedback mechanism, in the form of a reflecting boundary at the inner and/or outer edge of the torus.

Only very recently the nonlinear growth and saturation of the Papaloizou–Pringle instability in black hole–torus systems has been explored in three-dimensional numerical simulations in full general relativity [55] (see [56–58] for previous investigations neglecting the spacetime dynamics; see also [59] for numerical relativity simulations involving only constant angular momentum models and short evolution times). The simulations of [55] have shown that the instability sets in for a wide range of black hole–torus systems, and that the resulting non-axisymmetric structure is maintained for dozens of orbital periods well beyond the saturation of the instability. As a result, such systems can be strong sources of detectable gravitational waves for the upcoming detectors.

As an example, figure 2 illustrates the non-axisymmetric morphological features present in the tori of the two angular momentum profiles considered by [55], once the instability has saturated and a stationary accretion phase has been reached. As found in earlier test-fluid simulations in general relativity [57] the manifestation of the Papaloizou–Pringle instability is in the form of counter-rotating epicyclic vortices, or “planets”, with m planets emerging from the growth of a mode of order m . The instability grows exponentially with time, with the $m = 1$ mode, whose presence is apparent in the figure, being the fastest growing mode.

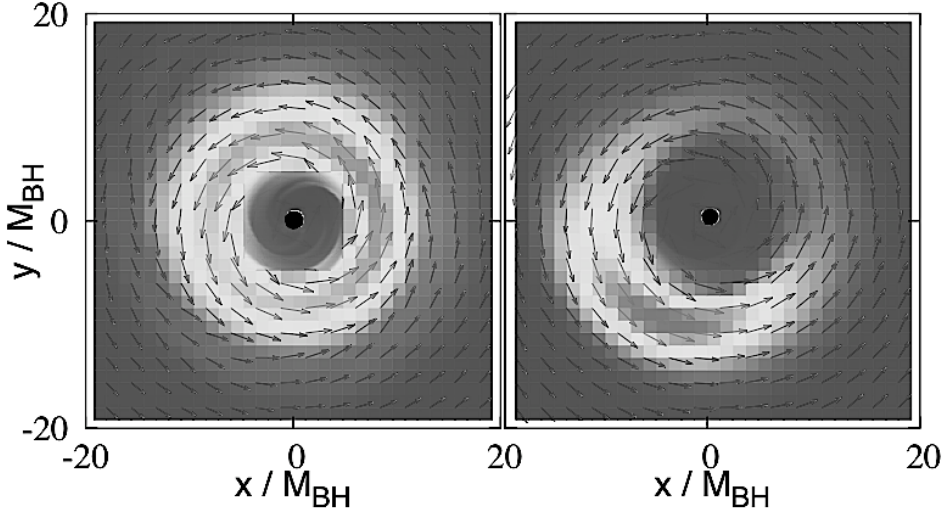


Fig. 2. Snapshots of the rest-mass density distribution on the equatorial plane for a constant angular momentum disk at $t = 15.11 t_{\text{orb}}$ (left: t_{orb} stands for the orbital timescale) and a non-constant angular momentum disk at $t = 20.02 t_{\text{orb}}$ (right). Vectors show the velocity fields, and black filled circles around the centres show the region inside the apparent horizons of the black holes. By the time of the evolution plotted the existence of $m = 1$ structures in the disk is manifest in both models. See [55] for further details.

4. Summary

This paper has presented an overview of numerical relativity simulations of binary neutron star mergers and the evolution of black hole–torus systems. Such numerical work is based upon a basic theoretical framework which comprises the Einstein’s equations for the gravitational field and the hydrodynamic equations for the evolution of the matter fields. The most well-established formulations for both systems of equations have been discussed and presented in some detail, along with the numerical methods best suited for their numerical solution — high-order finite-differencing for the case of the gravitational field equations and high-resolution shock-capturing schemes for the case of the relativistic Euler equations.

Among the results considered we have reviewed the outcome of a BNS merger event depending on the initial total mass and EOS of the binary. The formation of a HMNS followed by the appearance of a black hole–torus system show strong dependence on the total mass and EOS, and the same applies to the associated gravitational waveforms. The increasing body of work on the subject proves that large-scale tori with large masses (~ 0.1 – 0.2 times the total mass of the system) can be produced as the result of the

inspiral and merger of unequal-mass BNS, providing the energy reservoir needed to power short-hard GRBs. When analysing the evolution of the angular-momentum distribution in the tori, the existing simulations show no evidence for the onset of the runaway instability. However, on longer time scales non-axisymmetric (Papaloizou–Pringle) instabilities set in, the $m = 1$ mode being the fastest growing mode. The $m = 1$ structure (planet) survives with significant amplitude well beyond the nonlinear growth and saturation of the instability, which leads to the emission of quasi-periodic gravitational waves of large amplitude. Advanced detectors may reveal such kind of gravitational wave source. For stellar mass black holes, these results suggest that the so-called collapsar hypothesis of GRBs may be verified via observation of gravitational waves.

I am very grateful to the Organizers of the LII Cracow School of Theoretical Physics, and, in particular, to Prof. Michał Przaszałowicz, for the invitation to present the contents of this paper as a series of two lectures in the School. The numerical results presented in this paper have been obtained in collaboration with a number of colleagues — L. Baiotti, B. Giacomazzo, K. Kiuchi, D. Link, P. Montero, L. Rezzolla, and M. Shibata — to whom I am most grateful. This work has been supported by the Spanish MICINN (under grant AYA 2010-21097-C03-01) and by a VESF fellowship from the European Gravitational Observatory (EGO-DIR-69-2010).

REFERENCES

- [1] M. Shibata, K. Taniguchi, *Phys. Rev.* **D73**, 064027 (2006).
- [2] L. Baiotti, B. Giacomazzo, L. Rezzolla, *Phys. Rev.* **D78**, 084033 (2008).
- [3] M. Anderson *et al.*, *Phys. Rev.* **D77**, 024006 (2008).
- [4] M. Anderson *et al.*, *Phys. Rev. Lett.* **100**, 191101 (2008).
- [5] L. Baiotti, B. Giacomazzo, L. Rezzolla, *Class. Quantum Grav.* **26**, 114005 (2009).
- [6] K. Kiuchi, Y. Sekiguchi, M. Shibata, K. Taniguchi, *Phys. Rev.* **D80**, 064037 (2009).
- [7] B. Giacomazzo, L. Baiotti, L. Rezzolla, *Mon. Not. R. Astron. Soc.: Lett.* **399**, L164 (2009).
- [8] K. Kiuchi, Y. Sekiguchi, M. Shibata, K. Taniguchi, *Phys. Rev. Lett.* **104**, 141101 (2010).
- [9] L. Rezzolla *et al.*, *Class. Quantum Grav.* **27**, 114105 (2010).
- [10] L. Rezzolla *et al.*, *Astrophys. J. Lett.* **732**, L6 (2011).
- [11] R. Narayan, B. Paczynski, T. Piran, *Astrophys. J. Lett.* **395**, L83 (1992).

- [12] B. Zhang, P. Meszaros, *Int. J. Mod. Phys. A* **19**, 2385 (2004).
- [13] T. Piran, *Rev. Mod. Phys.* **76**, 1143 (2004).
- [14] J.A. Font, *Living Rev. Relativity* **11**, 7 (2008).
- [15] J. Faber, F. Rasio, *Living Rev. Relativity* **15**, 8 (2012).
- [16] M. Alcubierre, *Introduction to 3+1 Numerical Relativity*, Oxford University Press, USA, 2008.
- [17] A.M. Anile, *Relativistic Fluids and Magneto-fluids*, Cambridge University Press, 1989.
- [18] F. Banyuls *et al.*, *Astrophys. J.* **476**, 221 (1997).
- [19] L. Antón *et al.*, *Astrophys. J.* **637**, 296 (2006).
- [20] J. Wilson, *Astrophys. J.* **173**, 431 (1972).
- [21] J.M. Martí, J.M. Ibáñez, J.A. Miralles, *Phys. Rev.* **D43**, 3794 (1991).
- [22] F. Eulerink, G. Mellema, *Astron. Astrophys. Suppl. Ser.* **110**, 587 (1995).
- [23] P. Papadopoulos, J.A. Font, *Phys. Rev.* **D61**, 024015 (1999).
- [24] J.A. Font, J.M. Ibáñez, J.M. Martí, A. Marquina, *Astron. Astrophys.* **282**, 304 (1994).
- [25] A. Lichnerowicz, *J. Math. Pures et Appl.* **23**, 37 (1944).
- [26] R. Arnowitt, S. Deser, C.W. Misner, in: *Gravitation: An Introduction to Current Research*, L. Witten (ed.), pp. 227–265, Wiley, New York, USA, 1962.
- [27] J.W. York Jr., in: *Sources of Gravitational Radiation*, Proceedings of the Battelle Seattle Workshop, July 24–August 4, 1978, L.L. Smarr (ed.), pp. 83–126, Cambridge University Press, Cambridge, U.K.; New York, USA, 1979.
- [28] Y. Choquet-Bruhat, in: *Gravitation: An Introduction to Current Research*, L. Witten (ed.), pp. 68–130, Wiley, New York, USA, 1962.
- [29] T. Nakamura, K. Oohara, Y. Kojima, *Prog. Theor. Phys. Suppl.* **90**, 1 (1987).
- [30] M. Shibata, T. Nakamura, *Phys. Rev.* **D52**, 5428 (1995).
- [31] T.W. Baumgarte, S.L. Shapiro, *Phys. Rev.* **D59**, 024007 (1999).
- [32] J.J. Monaghan, *Annu. Rev. Astron. Astrophys.* **30**, 543 (1992).
- [33] E.F. Toro, *Riemann Solvers and Numerical Methods for Fluid Dynamics*, Springer Verlag, 1997.
- [34] J.M. Martí, E. Müller, *Living Rev. Relativity* **6**, 7 (2003).
- [35] J.M. Martí, E. Müller, *J. Fluid Mech.* **258**, 317 (1994).
- [36] J.A. Pons, J.M. Martí, E. Müller, *J. Fluid Mech.* **422**, 125 (2000).
- [37] F. Löffler *et al.*, *Class. Quantum Grav.* **29**, 115001 (2012).
- [38] M. Shibata, *Phys. Rev.* **D60**, 104052 (1999).
- [39] M. Shibata, K. Uryū, *Phys. Rev.* **D61**, 064001 (2000).
- [40] M. Shibata, K. Uryū, *Prog. Theor. Phys.* **107**, 265 (2002).
- [41] Y. Sekiguchi, K. Kiuchi, K. Kyutoku, M. Shibata, *Phys. Rev. Lett.* **107**,

- 051102 (2011).
- [42] Y. Sekiguchi, K. Kiuchi, K. Kyutoku, M. Shibata, *Phys. Rev. Lett.* **107**, 211101 (2011).
 - [43] M. Shibata, K. Taniguchi, K. Uryū, *Phys. Rev.* **D68**, 084020 (2003).
 - [44] M.J. Rees, *Annu. Rev. Astron. Astrophys.* **22**, 471 (1984).
 - [45] M. Shibata, S.L. Shapiro, *Astrophys. J. Lett.* **572**, L39 (2002).
 - [46] A. Heger *et al.*, *Astrophys. J.* **591**, 288 (2003).
 - [47] S.E. Woosley, *Astrophys. J.* **405**, 273 (1993).
 - [48] M.J. Rees, P. Meszaros, *Astrophys. J. Lett.* **430**, L93 (1994).
 - [49] M.A. Abramowicz, M. Calvani, L. Nobili, *Nature* **302**, 597 (1983).
 - [50] J.A. Font, F. Daigne, *Mon. Not. R. Astron. Soc.* **334**, 383 (2002).
 - [51] F. Daigne, J.A. Font, *Mon. Not. R. Astron. Soc.* **349**, 841 (2004).
 - [52] P.J. Montero, J.A. Font, M. Shibata, *Phys. Rev. Lett.* **104**, 191101 (2010).
 - [53] M. Shibata, *Phys. Rev.* **D76**, 064035 (2007).
 - [54] J.C.B. Papaloizou, J.E. Pringle, *Mon. Not. R. Astron. Soc.* **208**, 721 (1984).
 - [55] K. Kiuchi, M. Shibata, P.J. Montero, J.A. Font, *Phys. Rev. Lett.* **106**, 251102 (2011).
 - [56] O.M. Blaes, J.F. Hawley, *Astrophys. J.* **326**, 277 (1988).
 - [57] J.F. Hawley, *Astrophys. J.* **381**, 496 (1991).
 - [58] J. de Villiers, J.F. Hawley, *Astrophys. J.* **577**, 866 (2002).
 - [59] O. Korobkin *et al.*, *Phys. Rev.* **D83**, 043007 (2011).